Electronic Supplementary Material (ESI) for Physical Chemistry Chemical Physics.

Supporting Information

Understanding the influence of secondary building units on the thermal conductivity of metal-organic frameworks via high-throughput computational screening

Yuanchuang Lin [a], Ruihuan Cheng [c], Tiangui Liang [a], Weixiong Wu [a], Song Li [, b] and Wei Li [*, a]*

a Energy & Electricity Research Center, Jinan University, Zhuhai, 519070, China

b Department of New Energy Science and Engineering, School of Energy and Power Engineering, Huazhong University of Science and Technology, Wuhan 430074, China

c Department of Mechanical Engineering, The University of HongKong, Pokfulam Road, HongKong SAR 999077, China

Corresponding authors

Email: weili@jnu.edu.cn; songli@hust.edu.cn

Noted: The table containing all the thermal conductivity results and related parameters were provided at:

https://github.com/linyuanchuang/MOFs_structures_thermalconductivity_relationship

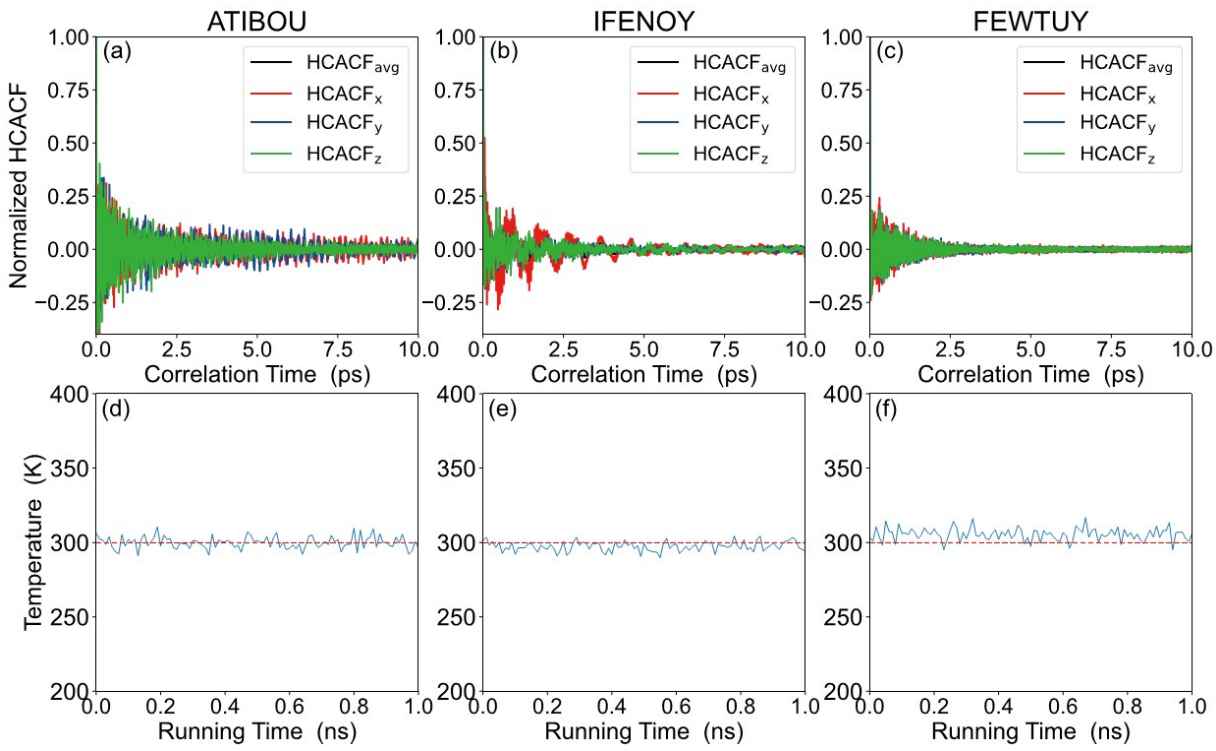

Figure S1. The normalized HCACF as a function of correlation time in the *x* (red), *y* (blue), *z* directions (green), respectively, for the (a)ATIBOU, (b)IFENOY, and (c)FEWTUY at 300 K and 1 bar. (d-f) represent the variation of temperature with time for the ATIBOU, IFENOY, and FEWTUY, respectively, under the NVE ensemble.

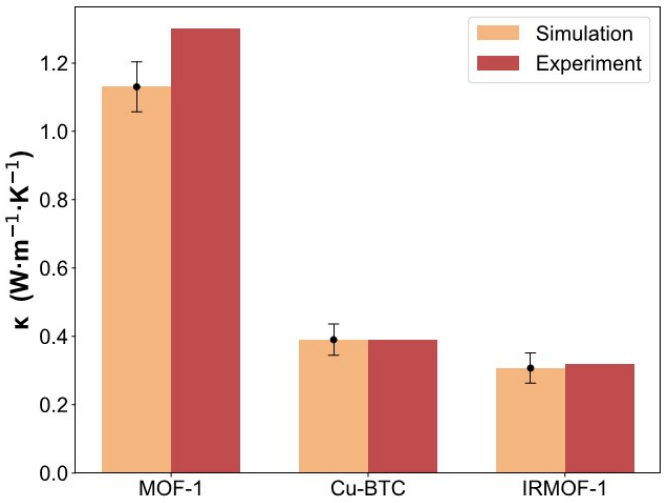

Figure S2. Comparison of simulation and experimental thermal conductivity for MOF-1, Cu-BTC, and IRMOF-1, in which the extended charge equilibration (Eqeq) method was used for MOF-1.

Table S1. MOFs with LCD between 11 Å and 12 Å and a VF of about 0.7.

MOF	ASA (m^2/g)	LCD (Å)	VF	Density (g/cm^3)	V_a (cm^3/g)	κ (W m^{-1} K^{-1})

MgMOF-74	1681.25	11.86	0.730	0.883	0.675	1.606
CUVTUJ	1222.81	11.68	0.710	1.176	0.492	1.798
Co-DOBDC	1201.25	11.61	0.718	1.181	0.488	2.048
CAXWEF	1335.22	11.60	0.703	1.145	0.496	2.262
CAXWIJ	1270.71	11.56	0.704	1.143	0.501	2.452
Mg-DOBDC	1609.06	11.70	0.739	0.922	0.645	2.612
CAXVUU	1329.9	11.30	0.697	1.147	0.492	2.746
CAXWAB	1276.81	11.50	0.701	1.145	0.498	2.874
CAXVII	1336.12	11.64	0.700	1.124	0.511	3.118
Ni-DOBDC	1217.07	11.45	0.707	1.194	0.493	3.223

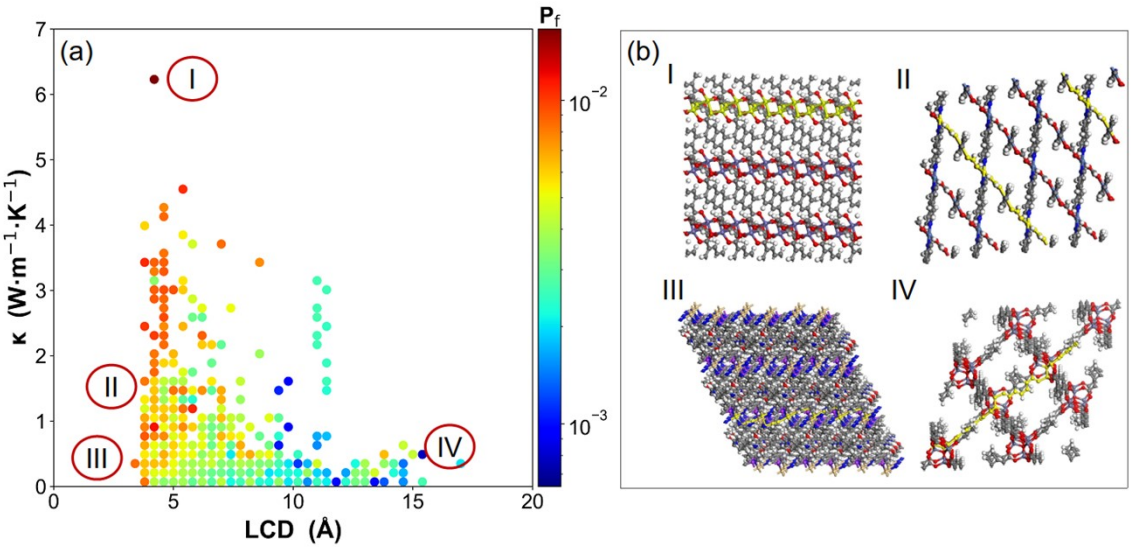

Figure S3. (a) The figure on the left illustrates where each structure is located, colored by P_f: (I) high thermal conductivity with large P_f, (II) medium thermal conductivity with large P_f, (III) low thermal conductivity with large P_f, (IV) low thermal conductivity with small P_f. Each plot is divided into 50 × 50 bins which are illustrated by a filled circle, whose color represents the averaged property across all MOFs in that bin. (b) The right panel shows schematics of structures I (TONBII), II (FIFPAM01), III (PAPXUB), and IV (IRMOF-6), where the yellow-colored atoms represent the optimal heat transfer pathway.

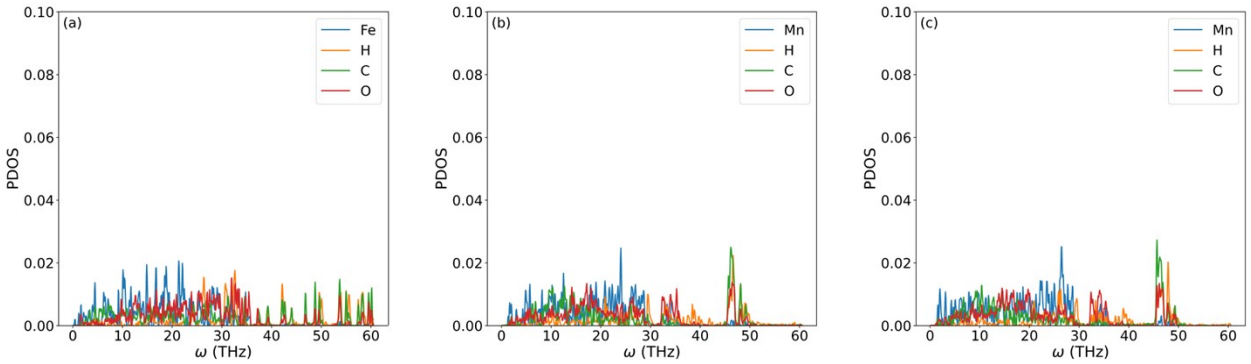

Figure S4. The partial density of states (PDOS) of high thermal conductivity MOFs, (a) TONBII (Top1, Fe element-based), (b) WICGEV (Top3, Mn element-based), (c) ATIBOU (Top4, Mn element-based).

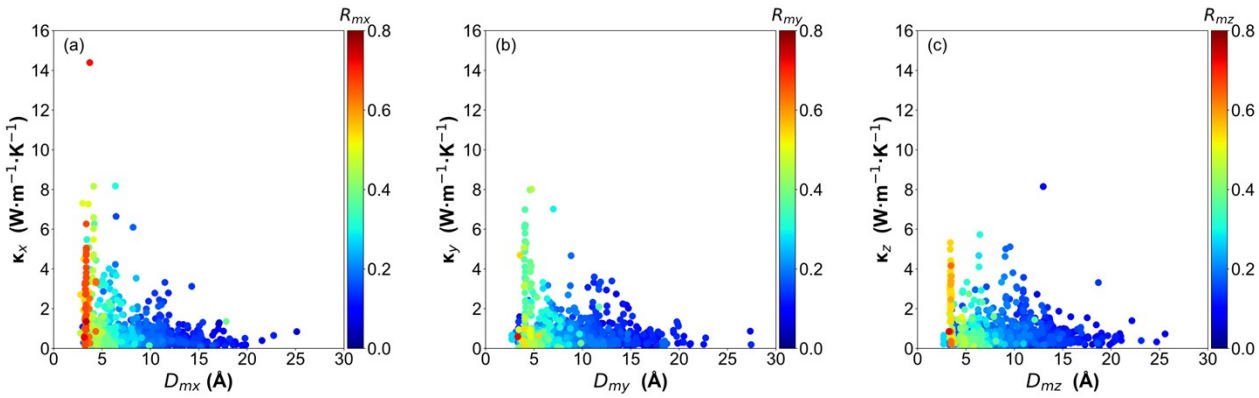

Figure S5. The relationship between metal atom distances and thermal conductivity in the *x*, *y*, and *z* directions of heat transfer pathways, colored by the ratio of metal atoms, which (a), (b), and (c) represent the *x*, *y*, and *z* directions, respectively.

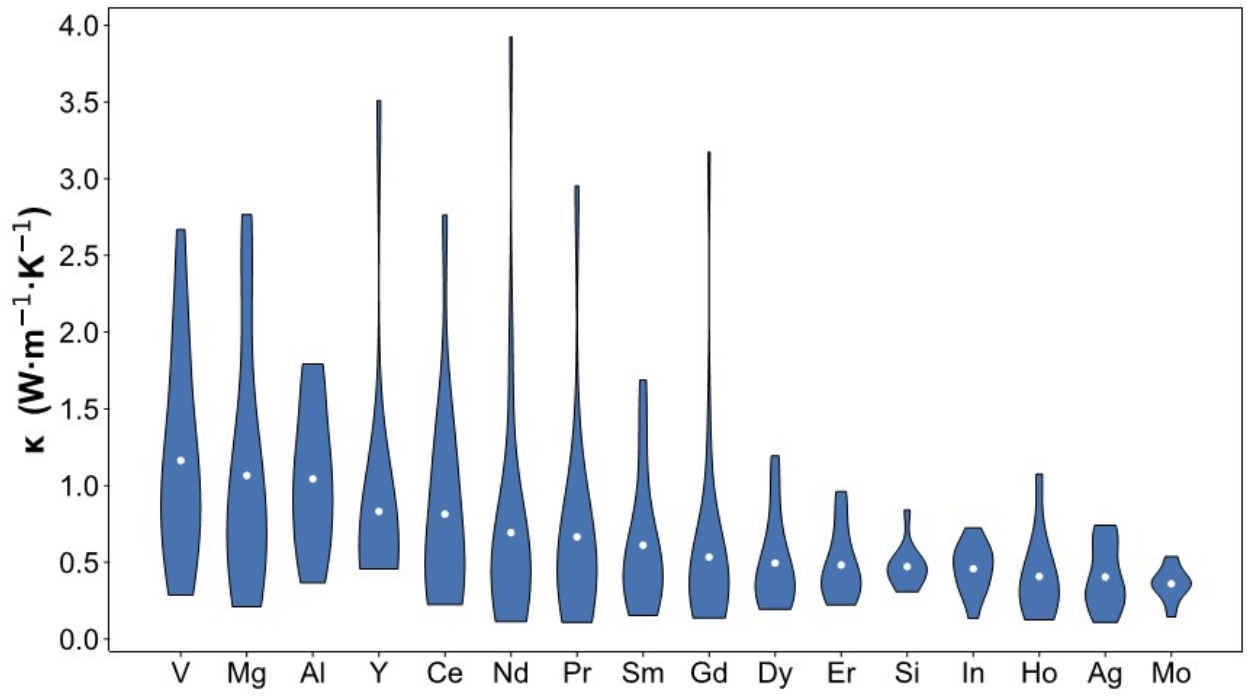

Figure S6. Violin plots of the thermal conductivities of MOFs containing different types of metals (Only metal types with more than 10 samples and less than 30 samples are shown).

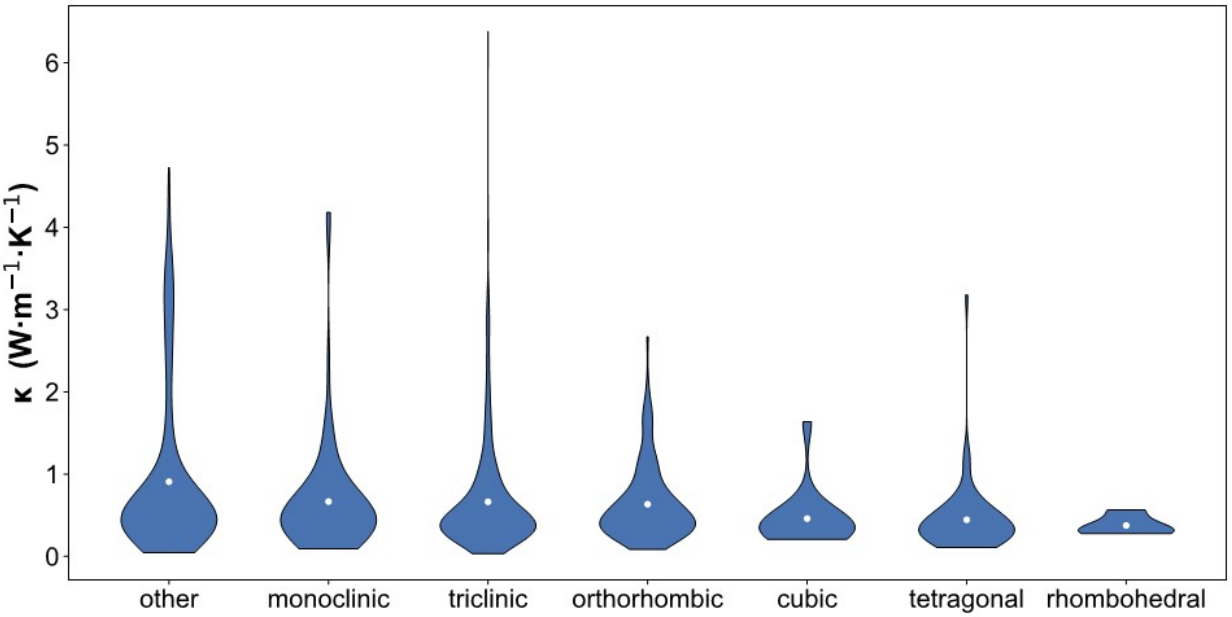

Figure S7. Violin plots of thermal conductivity for MOFs of different crystal types.

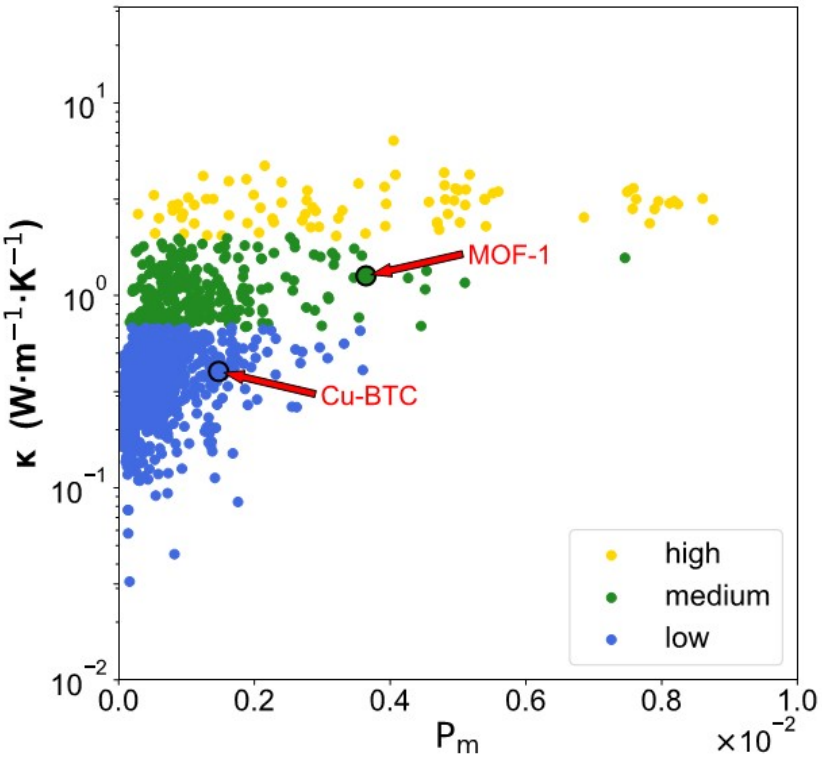

Figure S8. The relationship between P_m and thermal conductivity, including the MOF-1 and Cu-BTC.

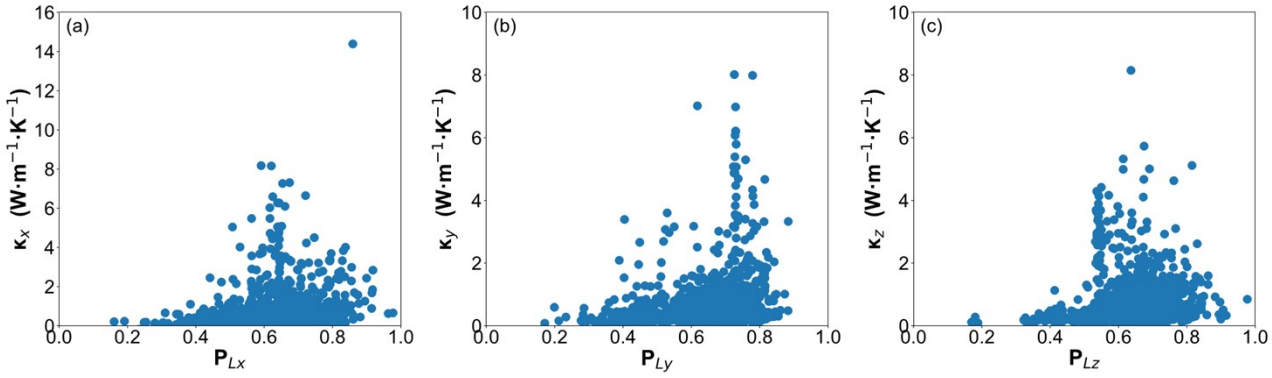

Figure S9. Thermal conductivity of 1214 MOFs as a function of P_L in the (a) *x*, (b) *y*, (c) and *z* direction.

Table S2. Pearson correlation coefficients between thermal conductivity and various factors.

Factors	Pearson correlation coefficients
P_m	0.68
R_m	0.52
P_f	0.42
N_i/S_i	0.31
ρ	0.29
P_L	0.17
LCD	-0.22
V_a	-0.23
VF	-0.24

ASA		-0.27

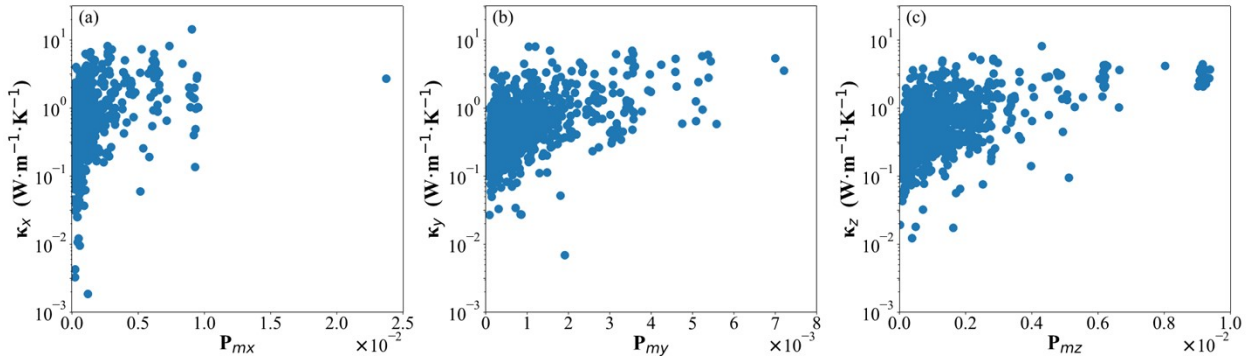

Figure S10. Thermal conductivity of 1214 MOFs as a function of P_m in the (a) *x*, (b) *y*, (c) and *z* direction.

Table S3. The structural characteristics, pathway factor, and thermal conductivity of TONBII.

Parameter	Value	Unit
ASA	265.5	m^2/g
LCD	4.6	Å
VF	0.25	-
PLD	4.23	Å
ρ	1.6	g/cm^3
V_a	0.10	cm^3/g
Metal type	Fe	-
P_{mx}	0.005257	-
P_{my}	0.00233	-
P_{mz}	0.004302	-
P_m	0.00405	-
κ_x	7.309341	W m^{-1} K^{-1}
κ_y	3.393083	W m^{-1} K^{-1}
κ_z	8.148788	W m^{-1} K^{-1}
κ	6.378039	W m^{-1} K^{-1}

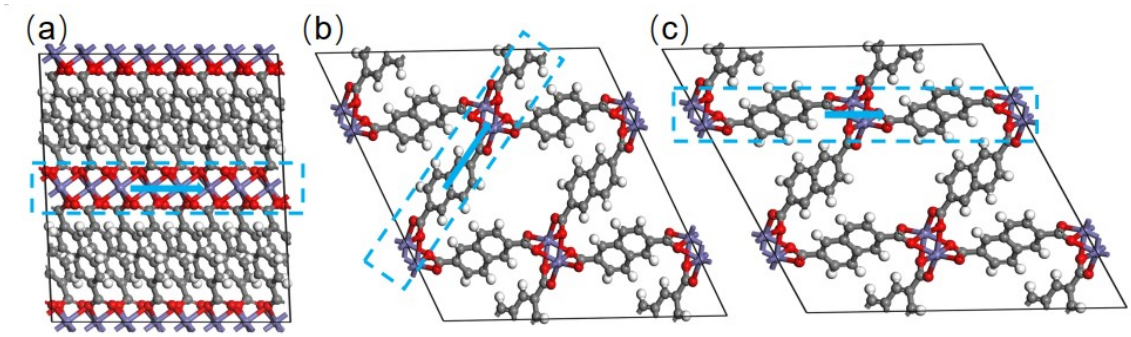

Figure S11. The optimal heat transfer pathway (highlighted in blue) in the (a) *x*, (b) *y*, (c) *z* direction.

Table S4. The average values of various parameters along the *x* direction for the three types of topologies, *met*, *rna*, and *pcu*.

Topology	Direction	N_i	S_i	P_{Li}	R_{mi}	κ_{Ami}	P_{mi}
met	x	12.36	1043	0.65	0.62	1.35	6.5×10^{-3}
	y	7.96	923	0.74	0.38	1.36	3.2×10^{-3}
	z	17.36	1061	0.56	0.51	1.34	6.4×10^{-3}
rna	x	6.78	989	0.67	0.35	1.56	2.3×10^{-3}
	y	16.25	948	0.60	0.15	0.89	1.5×10^{-3}
	z	18.56	894	0.68	0.17	1.23	2.4×10^{-3}
pcu	x	7.07	1097	0.61	0.16	0.69	4.6×10^{-4}
	y	7.61	1107	0.63	0.17	0.65	4.5×10^{-4}
	z	8.74	1081	0.63	0.17	0.70	6.7×10^{-4}

Table S5. Proportions of different metal elements and their corresponding average thermal conductivity for each metal type in MOFs with *met*-type topology.

Metal Type	Proportion	Average Thermal Conductivity

Mn	42.22%	1.244
Co	11.11%	1.029
Fe	31.11%	1.893
Cu	4.44%	0.457
Cd	2.22%	0.433
Mg	6.67%	1.067
Zn	2.22%	0.521

Table S6. Proportions of different metal elements and their corresponding average thermal conductivity for each metal type in MOFs with *rna*-type topology.

Metal Type	Proportion	Average Thermal Conductivity
V	34.38%	1.164
Al	31.25%	1.044
Fe	18.75%	1.893
Cr	6.25%	1.034
Sc	3.13%	0.932
Ga	6.25%	0.829

Table S7. Proportions of different metal elements and their corresponding average thermal conductivity for each metal type in MOFs with *pcu*-type topology.

Metal Type	Proportion	Average Thermal Conductivity
Zn	46.49%	0.521
Mn	7.02%	1.244
Cu	4.39%	0.457
La	0.88%	0.660
Mg	5.26%	1.067

Co	7.89%	1.029
Fe	0.88%	1.893
Ni	1.75%	0.733
Pr	2.63%	0.666
Y	0.88%	0.832
Nd	2.63%	0.694
Gd	6.14%	0.534
Cd	6.14%	0.433
Sm	0.88%	0.612
Tm	1.75%	0.646
Ce	1.75%	0.815
Dy	1.75%	0.496
Ho	0.88%	0.409

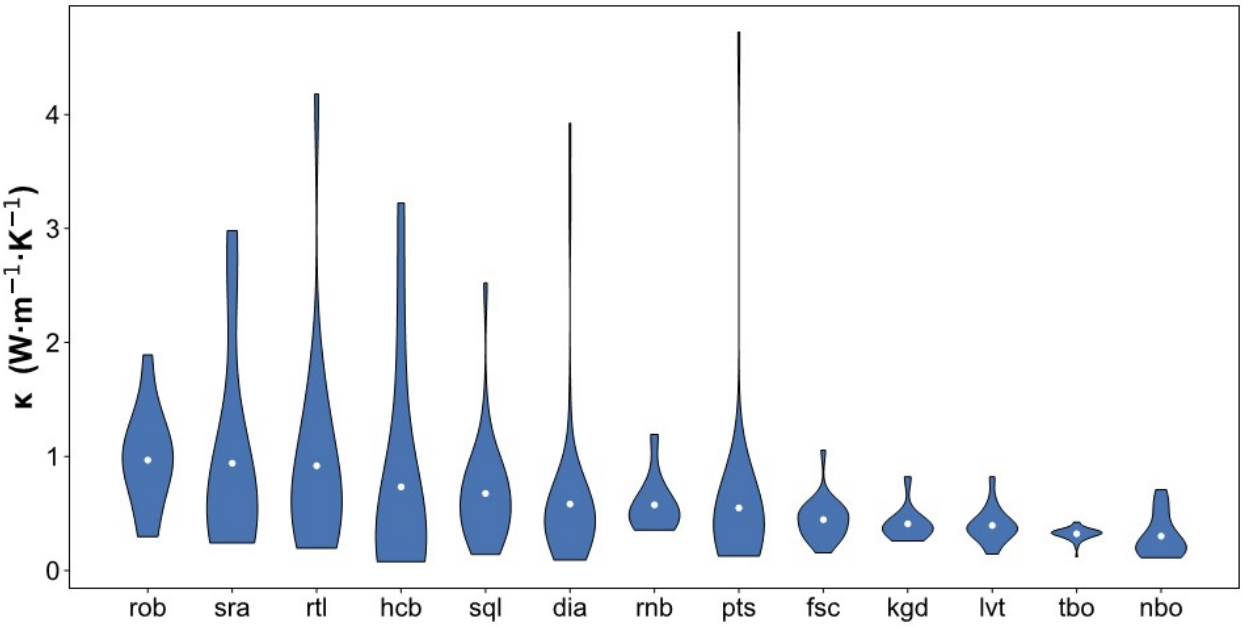

Figure S12. Violin plots of the thermal conductivities of MOFs with different topologies. Only topologies with a sample size exceeding 10 and excluding *met*, *rna*, and *pcu* topologies are displayed.

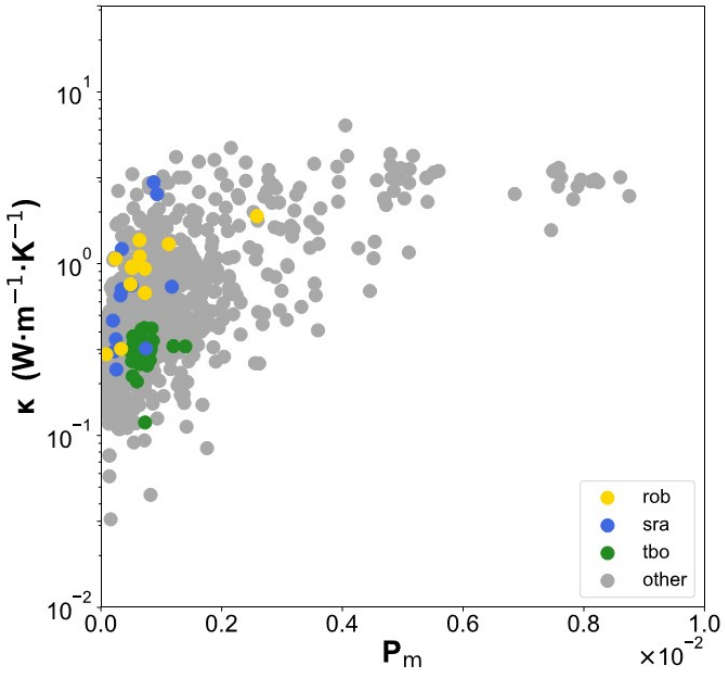

Figure S13. The distribution of thermal conductivity for MOFs with different topologies (*rob*, *sra*, *tbo*, and others).

Table S8. Pearson correlation coefficients between thermal conductivity and interaction parameters along the heat transfer pathway.

Interaction parameter	Pearson correlation coefficients
Aε	-0.27
Aσ	-0.46
A_harmonic	-0.28
A_pos_charge	0.27
A_neg_charge	-0.36
A_metal_charge	0.10
P_m /Aε	0.66
P_m /Aσ	0.68
Pm /A_harmonic	0.66
P_m *A_pos_charge	0.66
P_m*(-A_neg_charge)	0.66
P_m*A_metal_charge	0.59

P_m*B_{mi}	0.68

Notes: Aε, Aσ, A_harmonic, A_pos_charge, A_neg_charge, A_metal_charge, B_{mi} represent the average ε, σ, harmonic bond parameters, positive charge, negative charge, metal charge, average bond connected to metal atoms along the optimal heat transfer pathway.

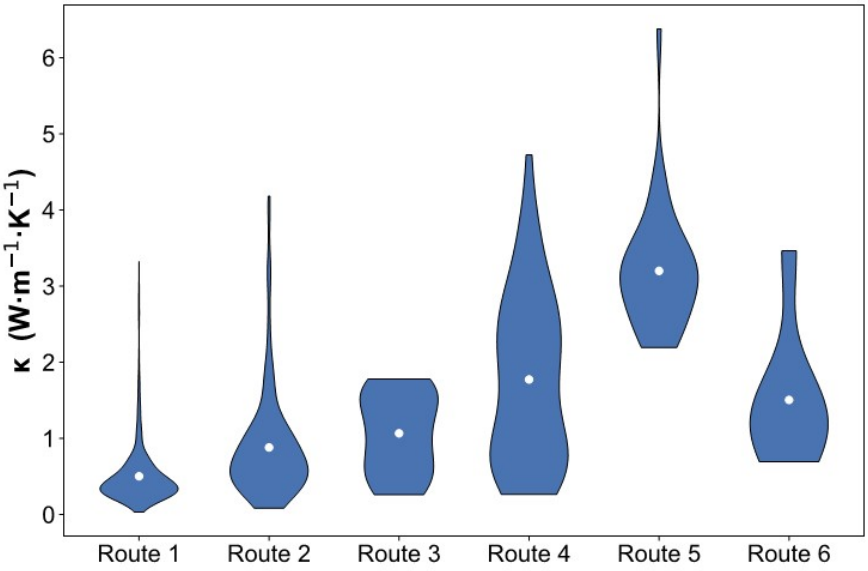

Figure S14. The distribution of thermal conductivity on the six routes.

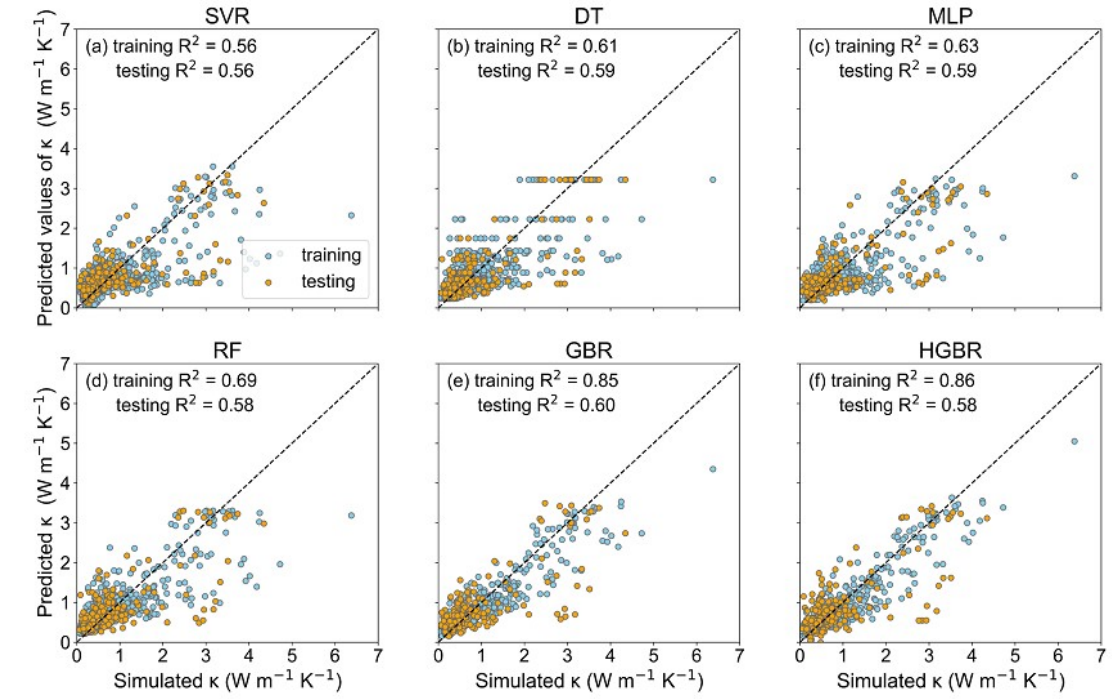

Figure S15. Machine learning for the training and test datasets for (a) SVR, (b) DT, (c) MLP, (d) RF, (e) GBR, and (f) HGBR, in which P_m, ASA, ρ, LCD, VF, Va, and PLD were used as descriptors.

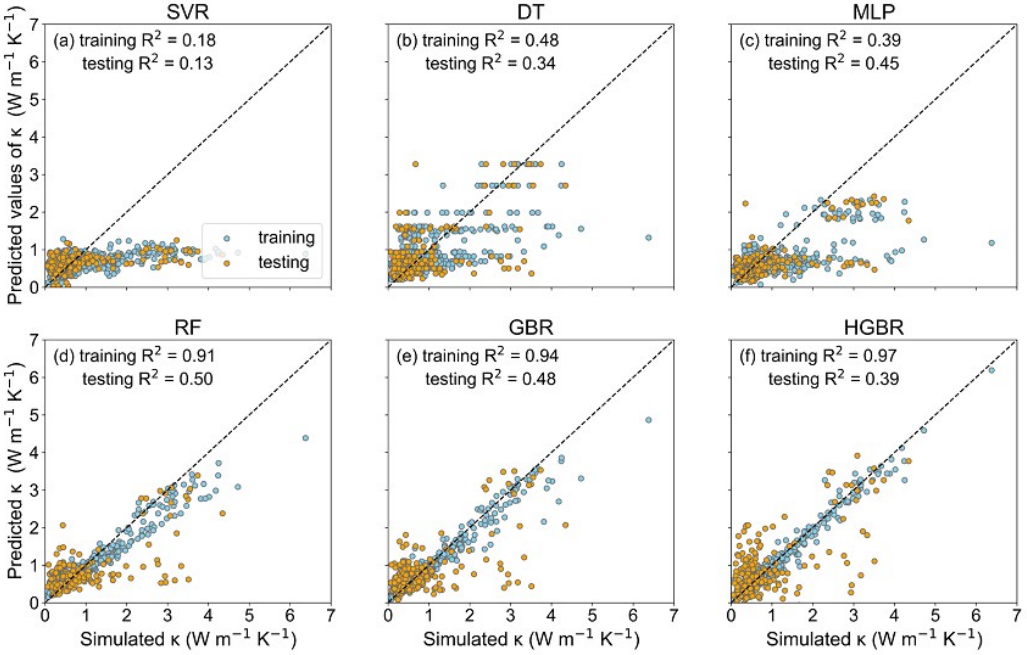

Figure S16. Machine learning for the training and test datasets for (a) SVR, (b) DT, (c) MLP, (d) RF, (e) GBR, and (f) HGBR, in which ASA, ρ, LCD, VF, Va, and PLD were used as descriptors.

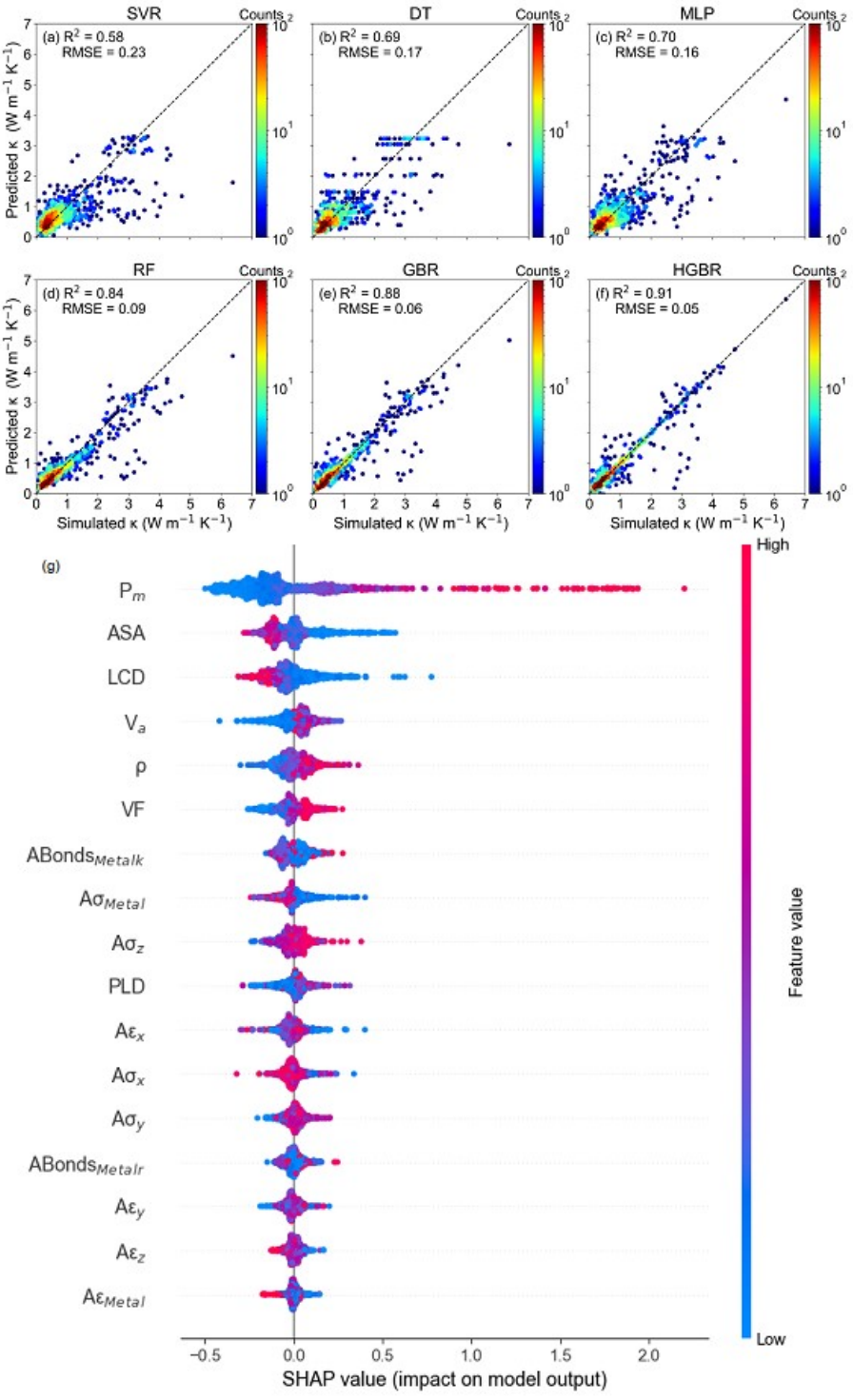

Figure S17. Predicted values of thermal conductivity by various machine learning algorithms, (a) SVR, (b) DT, (c) MLP, (d) RF, (e) GBR, and (f) HGBR. (g) The Shapley additive explanations (SHAP) values on thermal conductivity of 17 descriptors from the HGBR algorithm, including P_m, ASA, ρ, LCD, VF, V_a, PLD, $A\delta_x$, $A\varepsilon_x$, $A\delta_y$, $A\varepsilon_y$, $A\delta_z$, $A\varepsilon_z$, $A\delta_{metal}$, $A\varepsilon_{Metal}$, $Abonds_{Metalk}$, and $ABonds_{Metalr}$.

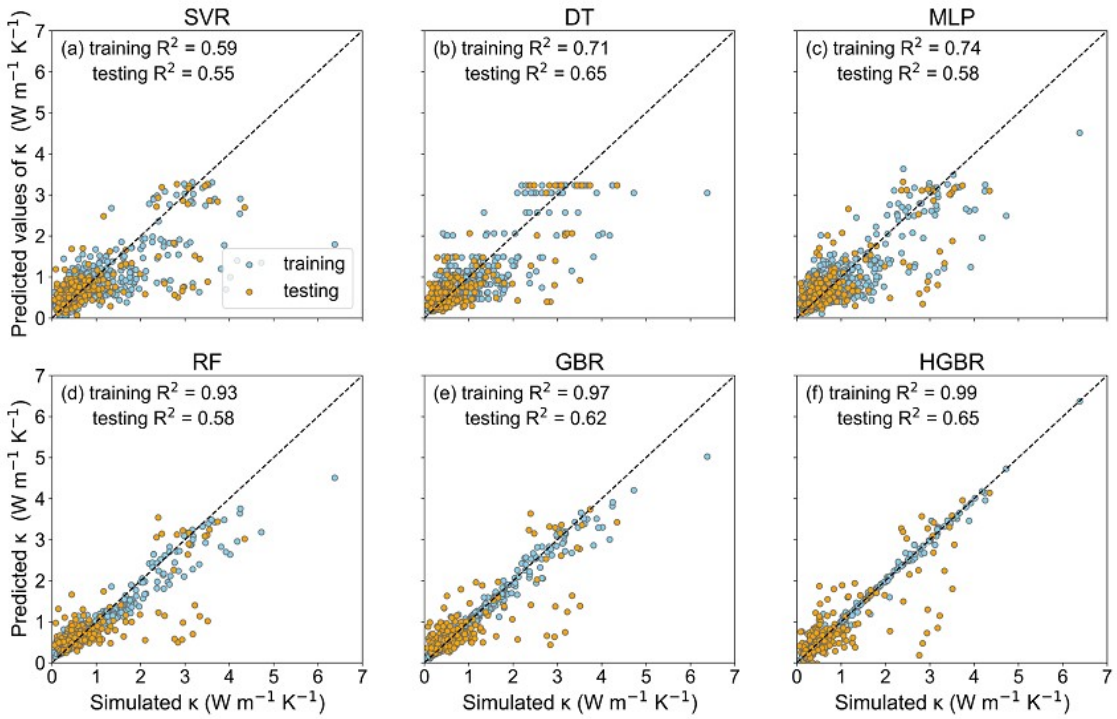

Figure S18. Machine learning for the training and test datasets for (a) SVR, (b) DT, (c) MLP, (d) RF, (e) GBR, and (f) HGBR, in which P_m, ASA, ρ, LCD, VF, V_a, PLD, $A\delta_x$, $A\varepsilon_x$, $A\delta_y$, $A\varepsilon_y$, $A\delta_z$, $A\varepsilon_z$, $A\delta_{metal}$, $A\varepsilon_{Metal}$, $Abonds_{Metalk}$, and $ABonds_{Metalr}$ were used as descriptors.

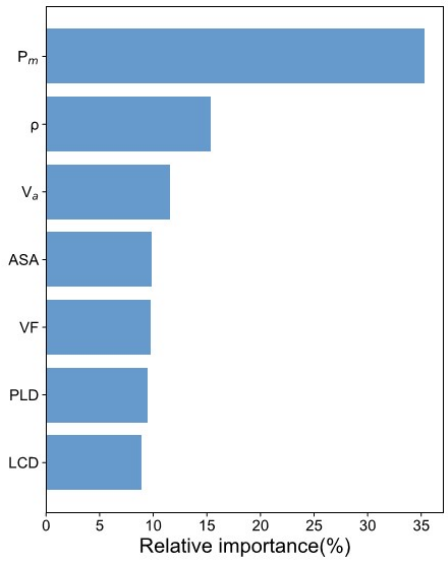

Figure S19. The relative importance of seven descriptors including P_m, ASA, ρ, LCD, VF, Va, and PLD on the thermal conductivity from the HGBR algorithm.